Monthly Notices
of the
ROYAL ASTRONOMICAL SOCIETY

Mon. Not. R. Astron. Soc. **416,** 493–500 (2011) doi:10.1111/j.1365-2966.2011.19061.x

Intermediate-age stars as the origin of low stellar velocity dispersion nuclear rings: the case of Mrk 1157

Rogério Riffel,[1]⋆ Rogemar A. Riffel,[2] Fabricio Ferrari[3] and Thaisa Storchi-Bergmann[1]

[1] *Instituto de Física, Universidade Federal do Rio Grande do Sul, CP 15051, 91501-970 Porto Alegre, RS, Brazil*
[2] *Departamento de Física, Centro de Ciências Naturais e Exatas, Universidade Federal de Santa Maria, 97105-900 Santa Maria, RS, Brazil*
[3] *Instituto de Matemática Estatística e Física, Universidade Federal de Rio Grande, CP 474, 96201-900 Rio Grande, RS, Brazil*

Accepted 2011 May 11. Received 2011 April 29; in original form 2011 January 28

ABSTRACT

We have used the Gemini Near-Infrared Integral-Field Spectrograph to map the age distribution of the stellar population in the inner 400 pc of the Seyfert 2 galaxy Mrk 1157 (NGC 591), at a spatial resolution of 35 pc. We have performed wavelet and principal component analysis on the data in order to remove instrumental signatures. An old stellar population component (age $\gtrsim$ 5 Gyr) is dominant within the inner $\approx$130 pc which we attribute to the galaxy bulge. Beyond this region, up to the borders of the observation field, young- to intermediate-age components (0.1–0.7 Gyr) dominate. As for Mrk 1066, previously studied by us, we find a spatial correlation between this intermediate-age component and a partial ring of low stellar velocity dispersion (σ_*). Low-σ_* nuclear rings have been observed in other active galaxies, and our results for Mrk 1157 and Mrk 1066 reveal that they are formed by intermediate-age stars. Such age is consistent with a scenario in which the origin of the low-σ_* rings is a past event which triggered an inflow of gas and formed stars which still keep the colder kinematics of the gas from which they have formed. No evidence for the presence of an unresolved featureless continuum and hot dust component – as found in Mrk1066 – is found for Mrk 1157.

Key words: methods: data analysis – galaxies: individual: Mrk 1157 – galaxies: individual: NGC 591 – galaxies: Seyfert – galaxies: stellar content.

1 INTRODUCTION

The coexistence of an active galactic nucleus (AGN) and young stars in the central region of Seyfert galaxies is a widely known phenomenon (see e.g. Storchi-Bergmann et al. 2000, 2001; González Delgado, Heckman & Leitherer 2001; Cid Fernandes et al. 2004; Asari et al. 2007; Dors et al. 2008), supporting the so-called AGN–starburst connection (e.g. Norman & Scoville 1988; Terlevich, Diaz & Terlevich 1990; Heckman et al. 1997; Heckman 2004; Riffel et al. 2009c). The above studies have pointed out that the main difference between the stellar population (SP) of active and non-active galaxies is an excess of intermediate-age stars in the former. In addition, near-infrared (NIR) SP studies have revealed that the continuum is also dominated by the contribution of intermediate-age SP components (SPCs, Riffel et al. 2007, 2009d, 2010; Martins et al. 2010). In the NIR, another component is commonly detected in the nuclear spectra of Seyfert galaxies: unresolved hot dust emission (Rodríguez-Ardila, Riffel & Pastoriza 2005; Rodríguez-Ardila et al. 2006; Riffel et al. 2009b,c,d). Thus, the study of the contribution of the SPs and other components to the circumnuclear continuum of active galaxies is a fundamental key in understanding the nature of their central engine.

Very recently, the use of integral field spectroscopy with adaptive optics at the Gemini North Telescope has allowed us to derive the contribution of distinct SPCs to the NIR spectra of active galaxies. In addition, we have mapped SPC spatial distributions and performed the first 2D SP synthesis in the NIR of the nuclear region of an active galaxy (Mrk 1066, Riffel et al. 2010). A spatial correlation between the intermediate-age SPC and a partial ring of low stellar velocity dispersion (σ_*) was found, supporting the interpretation that the low-σ_* structures commonly observed in the inner few hundred parsecs of Seyfert galaxies are due to colder regions with more recent star formation than the underlying bulge (Barbosa et al. 2006; Riffel et al. 2008a, 2009a; Riffel & Storchi-Bergmann 2011). Using a different method – modelling the Brγ equivalent width, supernova rate and mass-to-light ratio – Davies et al. (2007) have quantified the star formation history in the centre of nine nearby Seyfert galaxies using their STARS code. They found that the ages of the stars which contribute most to the NIR continuum lie in the

⋆E-mail: riffel@ufrgs.br

range 10–30 Myr, pointing out that these ages should be considered only as 'characteristic', as they have not performed a proper spectral synthesis, suggesting that there may be simultaneously two or more SPs that are not coeval (Davies et al. 2007, 2006).

As part of an ongoing project aimed at mapping the 2D age distribution of the NIR SP in the inner few hundred parsecs of Seyfert galaxies, we present the NIR SP synthesis of the Seyfert 2 galaxy Mrk 1157 (NGC 591), an early-type barred spiral galaxy located at a distance $d = 61.1$ Mpc [from the NASA/IPAC Extragalactic Database (NED)], for which 1 arcsec corresponds to 296 pc at the galaxy. The near-IR gas excitation and kinematics as well as the stellar kinematics of the inner 450 pc of Mrk 1157 are discussed in Riffel & Storchi-Bergmann (in preparation) using the same data used here.

This paper is structured as follows. In Section 2, we describe the observations, data-reduction and cleaning procedures. The spectral-fitting procedures are discussed in Section 3. In Section 4, we present our results, which are discussed in Section 5. The conclusions are presented in Section 6.

2 THE DATA

2.1 Observations and data reduction

Mrk 1157 was observed with the Gemini Near-Infrared Integral-Field Spectrograph (NIFS) (McGregor et al. 2003) operating with the Gemini North Adaptive Optics system ALTAIR in 2009 September/October under the programme GN-2009B-Q-27, following the standard Object–Sky–Sky–Object dither sequence, with off-source sky positions since the target is extended, and individual exposure times of 550 s.

Two sets of observations with six on-source individual exposures were obtained at different spectral ranges: the first at the J band, centred at 1.25 μm and covering the spectral region from 1.14 to 1.36 μm, and the second at the K_1 band, centred at 2.3 μm, covering the spectral range from 2.10 to 2.53 μm. At the J band, the J_G5603 grating and ZJ_G0601 filter were used, resulting in a spectral resolution of ≈1.8 Å, as obtained from the measurement of the full width at half-maximum (FWHM) of ArXe arc lamp lines. The K_1-band observations were obtained using the Kl_G5607 grating and HK_G0603 filter and resulted in a spectral resolution of FWHM ≈ 3.5 Å.

The data reduction was accomplished using tasks contained in the NIFS package which is part of Gemini IRAF[1] package, as well as generic IRAF tasks. The reduction procedure included trimming of the images, flat-fielding, sky subtraction, wavelength and s-distortion calibrations. We have also removed the telluric bands and flux calibrated the frames by interpolating a blackbody function to the spectrum of the telluric standard star.

The angular resolution obtained from the FWHM of the spatial profile of the telluric standard star is 0.11 ± 0.02 arcsec for the J band and 0.12 ± 0.02 arcsec for the K_1 band, corresponding to 32.6 ± 5.9 and 35.5 ± 5.9 pc at the galaxy, respectively. Since the star has been observed for a shorter time than the galaxy, this value should be considered as a lower limit for the spatial resolution. Nevertheless, the performance of the ALTAIR for larger integration times (such as those used for the galaxy) in previous works by our group was found to be similar to the one reached in the observation of the star. In the case of NGC 4151, the spatial resolution of the galaxy is only 0.02 arcsec worse than those obtained from the FWHM of the brightness profile of the star (Storchi-Bergmann et al. 2009). For each band, individual data cubes were created at an angular sampling of 0.05×0.05 arcsec^2 and combined to a single data cube using the gemcombine IRAF task. More details about observations and data reduction can be found in Riffel & Storchi-Bergmann (in preparation).

[1] IRAF is distributed by the National Optical Astronomy Observatories, which are operated by the Association of Universities for Research in Astronomy, Inc., under cooperative agreement with the National Science Foundation.

2.2 Removing noise effects: the wavelet principal component analysis method

Because of the complexity of the instruments, hyperspectral data frequently contain instrumental signatures that cannot be removed with standard data-reduction techniques, and which in many cases contaminate the science data. The NIFS is no exception. The wavelet principal component analysis (WPCA) technique described below (a full account of the technique will be addressed in Ferrari et al., in preparation) can separate the instrumental fingerprint and, after its removal, allow the analysis of the 'clean' data.

2.2.1 Principal component analysis

Besides the relevant information, any set of data has some amount of redundant information and noise. The goal of the principal component analysis (PCA) is to find a new basis on which the data – the spectra from each spatial pixel – are expressed in a more meaningful way. The basis vectors – the principal components – are obtained by searching for the maximum variance in the data. There are as many vectors as the original variables, but usually the first few vectors contain most of the information of the data set: they provide a more concise description of the data. Often the physical content is restricted to few vectors and thus interpretation can be easier. Mathematically, we proceed as follows. In a basis where the variables are all uncorrelated (orthogonal), their covariance or correlation matrix is diagonal. We then find the principal components by diagonalizing the covariance or correlation matrix of the original data. In the case of the covariance matrix, the eigenvectors are the principal components and the eigenvalues are the variance associated with each of the eigenvectors. In the case of a hyperspectral cube, it is informative to measure the correlation between each principal component and the spectra in each spatial pixel: the tomograms. For example, tomogram 1 is the projection (scalar product) of eigenvector 1 and the spectra relative to each spatial pixel. For a full description on the method applied to astronomical data, see Steiner et al. (2009).

2.2.2 Discrete wavelet transform

The discrete wavelet transform (DWT) consists of describing a signal C_0 in terms of a smoothed component C_J and detail wavelet coefficients $\{W_j\}$ (Mallat 1999; Starck & Murtagh 2006):

$$C_0 = C_J + \sum_{j=1}^{J} W_j. \quad (1)$$

The maximum wavelet scale is J. In the *à trous* (i.e. with holes) algorithm (Starck & Murtagh 2006) used in this work, a series of smoothed versions $\{C_j\}$ of C_0 are calculated by convolving C_0 with scaled versions of a low-pass filter h. In this way, the term C_j is calculated by taking adjacent pixels from C_{j-1} that are 2^j pixels far

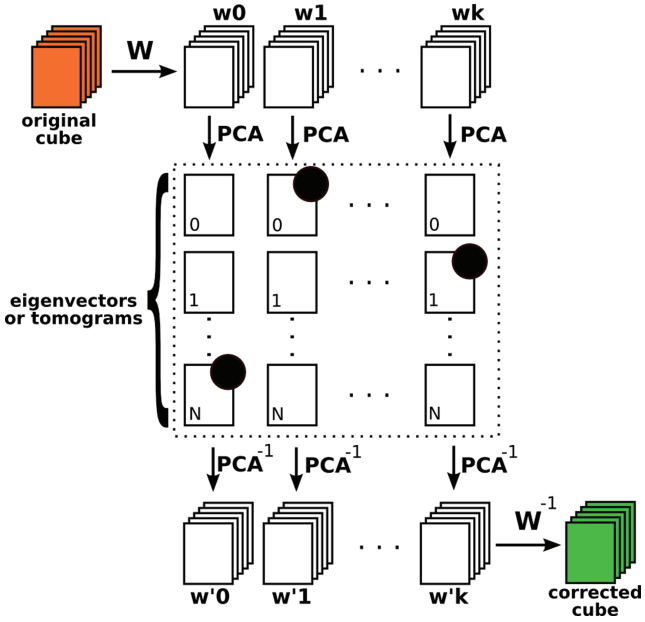

Figure 1. Wavelet and PCA combined: each spatial frame of the original data cube is first decomposed into wavelet (W) space and then the PCA is performed. After identifying and correcting for unwanted effects (e.g. instrumental signatures, fingerprints or noise), the cube is reconstructed in both PCA and wavelet spaces.

apart. We proceed in this way for each of the scale $j = 1 \ldots J$. After this, the DWT is obtained from the difference

$$W_j = C_j - C_{j-1}. \quad (2)$$

The wavelet coefficients $\{W_j\}$ now retain only details which are about 2^j in size, a multiresolution transform. The maximum scale J is mathematically arbitrary because, by virtue of equations (1) and (2), reconstruction is complete for any J. Physically, J is chosen so that the spatial frequencies of interest are lower than 2^J.

2.2.3 *The WPCA algorithm*

The idea behind the use of the wavelet and PCA transforms together is to decompose the original signal both in the wavelet and in the PCA space, select unwanted features and finally reconstruct the signal after eliminating these features. The algorithm is schematically shown in Fig. 1. The original data cube (orange) is first decomposed into wavelet scales $W_0, W_1, \ldots, W_k$. Then, the PCA is performed in each of the wavelet components, resulting in several eigenvectors for each scale. After removing those eigenvectors which contain unwanted structures (represented by the black dots in the figure), each of the wavelet components is restored with the PCA reconstruction, PCA^{-1}, and then the resulting corrected wavelets $W'_0, W'_1, \ldots, W'_k$ are combined to form the resulting corrected cube (green).

2.2.4 *Application to Mrk 1157*

Fig. 2 shows an example of the WPCA transform of the Mrk 1157 data cube. The columns are the wavelet decomposition of the original cube. In both Figs 1 and 2, the dotted rectangle represents the same kind of information: in each wavelet scale, a PCA is performed. The original information is completely represented in the wavelet space; thus, summing up all the components gives back the original data. The WPCA cleaning process is basically to identify the components (in wavelet and PCA spaces) which contain mostly instrumental signatures (i.e noise) and then to remove them and reconstruct the signal.

In the case of Mrk 1157 observations, the WPCA decomposition reveals that the W_0 tomograms are dominated by the instrumental signature (horizontal and vertical stripes in Fig. 2). That instrumental fingerprint can also be identified in the eigenvectors as high-frequency bumps (not shown) at the beginning and at the end of the spectra – the instrumental signature has a spatial and spectral behaviour. Thus, we remove W_0 and reconstruct the cube with $W_1 \ldots W_4$, W_C. We call the attention to the fact that we have analysed five wavelet scales and 20 principal components (with 20 eigenvectors and 20 tomograms; a total of 200 maps) to identify the instrumental signature. For the sake of brevity, in Fig. 2, we only show the first four principal components, which account for >95 per cent of the data variance.

The *clean* data cube was used to perform the SP analysis. The spatial resolutions of the J and K_l bands are very similar, allowing us to combine both data cubes into a single data cube and then perform the spectral synthesis. The combination was done using the scombine IRAF task at a spectral sampling of 2 Å. The astrometry was done using the peak of the continuum emission in both bands. We have rebinned the resulting data cube to a spatial sampling of 0.1 arcsec in order to reach a signal-to-noise ratio (S/N) high enough to obtain a reliable fit of the SP. The resulting S/N ranges from S/N $\approx$ 20 at the borders of the NIFS field to up to 120 at the nucleus. We used the wspectext IRAF task to convert the individual spectra of the final data cube to 784 ASCII files, used as input to the synthesis code. The observation field is $2.8 \times 2.8\,\mathrm{arcsec}^2$, which corresponds to $830 \times 830\,\mathrm{pc}^2$ at the galaxy.

3 SPECTRAL SYNTHESIS

Our main goal in this section is to map in detail the NIR spectral energy distribution components of the inner 400 pc of Mrk 1157. For this purpose, we fit simultaneously the underlying continuum of the J and K bands applying the method described in Riffel et al. (2009d) and summarized below.

In order to perform the SP synthesis, we use the STARLIGHT code (Cid Fernandes et al. 2004, 2005a; Mateus et al. 2006; Asari et al. 2007; Cid Fernandes et al. 2009). STARLIGHT fits the whole underlying spectrum, excluding emission lines and spurious data, mixing computational techniques originally developed for the semi-empirical population synthesis with ingredients from evolutionary synthesis models (Cid Fernandes et al. 2004, 2005a). Essentially, the code fits an observed spectrum, O_λ, with a combination, in different proportions, of $N_\star$ single SPs (SSPs). Extinction is parametrized by the V-band extinction A_V and modelled by STARLIGHT as due to foreground dust. In the fits, we use the Cardelli et al. (1989) extinction law. In order to model a spectrum M_λ, the code solves the following equation:

$$M_\lambda = M_{\lambda 0} \sum_{j=1}^{N_\star} x_j\, b_{j,\lambda}\, r_\lambda \otimes G(v_\star, \sigma_\star), \quad (3)$$

where $\boldsymbol{x}$ is the population vector, whose components $x_j\,(j = 1, \ldots, N_\star)$ represent the fractional contribution of each SSP in the base to the total synthetic flux at λ_0. $b_{j,\lambda}$ is the spectrum of the jth SSP of the base of elements normalized at λ_0, the reddening term is represented by $r_\lambda = 10^{-0.4(A_\lambda - A_{\lambda 0})}$, $M_{\lambda 0}$ is the synthetic flux at the normalization wavelength, $\otimes$ denotes the convolution operator and $G(v_\star, \sigma_\star)$ is the Gaussian distribution used to model the line-of-sight

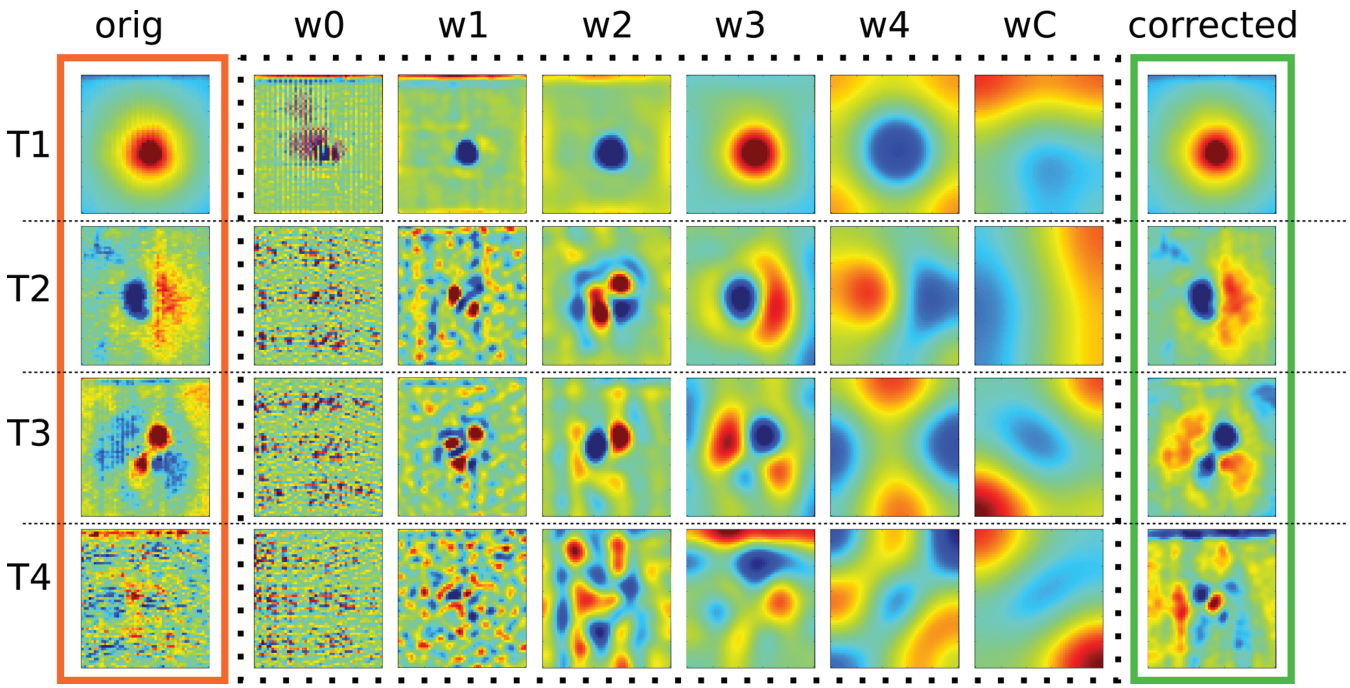

Figure 2. WPCA decomposition of the Mrk 1157 *J*-band data cube. The tomograms are separated in rows, from the top to bottom, tomograms 1 to 4. Original data (orange rectangle) are wavelet decomposed (black-dotted rectangle) into five scales plus continuum – $w_i, i = 0 \ldots 4$ and w_C – and then reconstructed without the first component w_0 (green rectangle). Colours in individual images are false to enhance details. The first four tomograms shown correspond to ∼95 per cent of the variance of the data cube. The figure frames have the same colour (rectangles) scheme as in Fig. 1. Colour may appear inverted because tomograms, as well as eigenvectors, are determined from the PCA, except for its sign.

stellar motions, which is centred at velocity $v_\star$ with dispersion $\sigma_\star$. However, note that due to the low spectral resolution of evolutionary population synthesis (EPS) models in the NIR, the $\sigma_\star$ values cannot be derived in a reliable way from the synthesis; thus, we do not use them. For details on $\sigma_\star$, see Section 4. The final fit is carried out by minimizing the equation

$$\chi^2 = \sum_\lambda [(O_\lambda - M_\lambda) w_\lambda]^2, \quad (4)$$

where emission lines and spurious features are excluded from the fit by fixing $w_\lambda = 0$.

In equation (3), the most important ingredient in SP synthesis is the base set, $b_{j,\lambda}$. As a default base, STARLIGHT uses the SSPs of Bruzual & Charlot (2003). However, these SSPs do not include the effect of the contribution of thermally pulsating asymptotic giant branch stars, whose contribution is enhanced in the NIR and crucial to model the SPs in this spectral region (see Riffel et al. 2007, 2008b, 2009d, 2010; Martins et al. 2010). Thus, we update the base using the Maraston (2005) EPS models as described in Riffel et al. (2009d). The base comprises SSP synthetic spectra covering 12 ages ($t = 0.01$, 0.03, 0.05, 0.1, 0.3, 0.5, 0.7, 1, 2, 5, 9 and 13 Gyr) and four metallicities ($Z = 0.02$, 0.5, 1 and $2\,Z_\odot$). We also include blackbody functions for temperatures in the range 700–1400 K in steps of 100 K (Riffel et al. 2009d) and a power law ($F_\nu \propto \nu^{-1.5}$) in order to account for possible contributions from dust emission (BB) and from a featureless continuum (FC), respectively, at the nucleus (e.g. Cid Fernandes et al. 2004). The same spectral base was used to map the age distribution of the SP in the inner 300 pc of Mrk 1066 (Riffel et al. 2010).

4 RESULTS

In Fig. 3 (top left-hand panel) , we show an optical image of Mrk 1157 taken with the Wide Field and Planetary Camera 2 (WFPC2) at the *Hubble Space Telescope* (*HST*) through the filter *F*606*W* (Malkan, Gorjian & Tam 1998). The 2.17-μm NIFS data cube continuum image is also shown in Fig. 3 (top right-hand panel). In order to illustrate the accuracy of our fits, we show in Fig. 3 (bottom panels) sample spectra, obtained within 0.1×0.1 arcsec^2 apertures for four distinct positions: the nucleus (position N marked in the top left-hand panel of Fig. 3) and 0.4 arcsec west (position A), 0.5 arcsec south-east (position B) and 0.8 arcsec north-east (position C) of the nucleus. The synthetic spectra were overplotted on the data as the dotted lines. As can be observed in this figure, the modelling of the SP reproduces very well the continuum/absorption spectra at all positions of Mrk 1157. Following Riffel et al. (2010), the observed and synthetic spectra were normalized at 2.12 μm, a region free of emission/absorption lines (Riffel et al. 2008b).

No contribution of the FC and/or BB components was necessary in order to reproduce the nuclear continuum in Mrk 1157. Similar result was obtained by Riffel et al. (2009d) when fitting the nuclear integrated spectrum of this source within a larger aperture ($r \simeq 200$ pc) over the 0.8–2.4 μm spectral region. We point out that the synthetic spectra were reddened using A_V derived from the synthesis (see Fig. 7 shown later).

Following Riffel et al. (2010, see also Riffel et al. 2009d; Cid Fernandes et al. 2004), we have binned the contribution of the SPCs (x_j) into a reduced population vector with four age ranges: young (x_y: $t \leq 100$ Myr); young intermediate (x_{yi}: $0.3 \leq t \leq 0.7$ Gyr), intermediate old (x_{io}: $1 \leq t \leq 2$ Gyr) and old (x_o: $5 \leq t \leq 13$ Gyr). In Fig. 4, we show the spatial distribution of the per cent flux contribution at 2.12 μm of the stars in each $\boldsymbol{x}$:

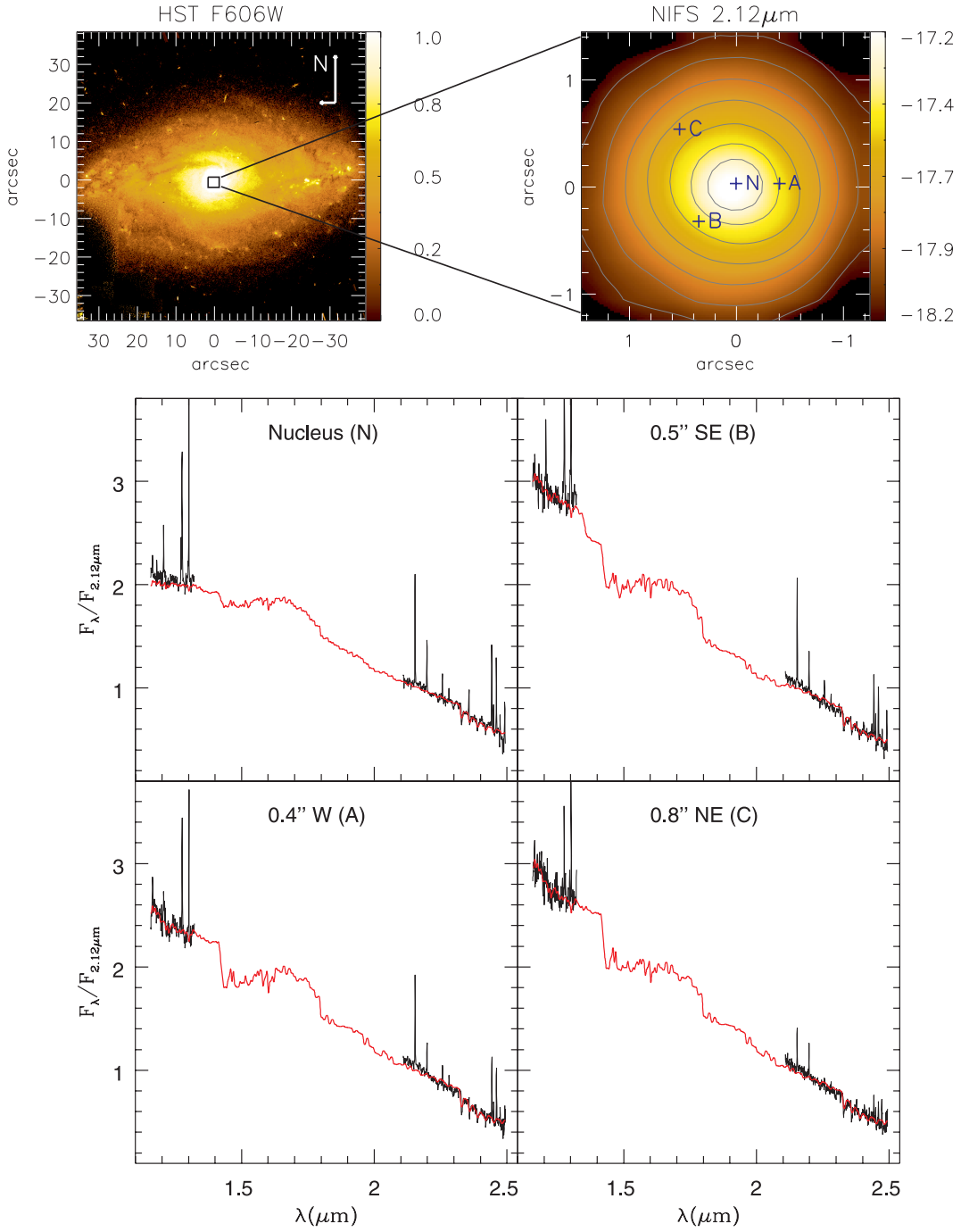

Figure 3. Top left-hand panel: *HST* WFPC2 continuum image of Mrk 1157 obtained through the filter *F606W* (Malkan et al. 1998). Top right-hand panel: 2.17-μm continuum image obtained from the NIFS data cube. The bottom left-hand panels show typical spectra obtained within a 0.25 × 0.25 arcsec^2 aperture for the nucleus and for a location at 0.4 arcsec north-west from it (position A). The box in the *HST* image shows the NIFS field of view. The bottom right-hand panels show typical spectra obtained within a 0.1 × 0.1 arcsec^2 aperture and the resulting fit of the SP for the positions marked in the top right-hand panel.

while in regions farther than $r \sim 0.8$ arcsec (240 pc) from the nucleus, the contribution of the young-intermediate SPCs reaches values of up to 100 per cent, closer to the nucleus, the contribution of this component is negligible. Within this region, the SP is dominated by the old component (≈50 per cent), closely surrounded ($r \lesssim 0.4$ arcsec) by an intermediate-old population (also ≈50 per cent). No signs of young SPs were detected close to the nucleus; however, a significant contribution (25–60 per cent) is found in regions farther than $r \sim 0.6$ arcsec.

The light-fraction SPC contributions depend on the normalization wavelength, and thus the comparison with results from other spectral regions should be done with caution (Riffel et al. 2011). However, a physical parameter which does not depend on the normalization point used in the fit is the stellar mass. The mass fraction of each population vector component is shown in Fig. 4 (young: m_y, young intermediate: m_{yi}, intermediate old: m_{io} and old population: m_o). The maps of the mass-weighted SPC follow a similar distribution to the light-weighted ones. However, in the former, the contribution

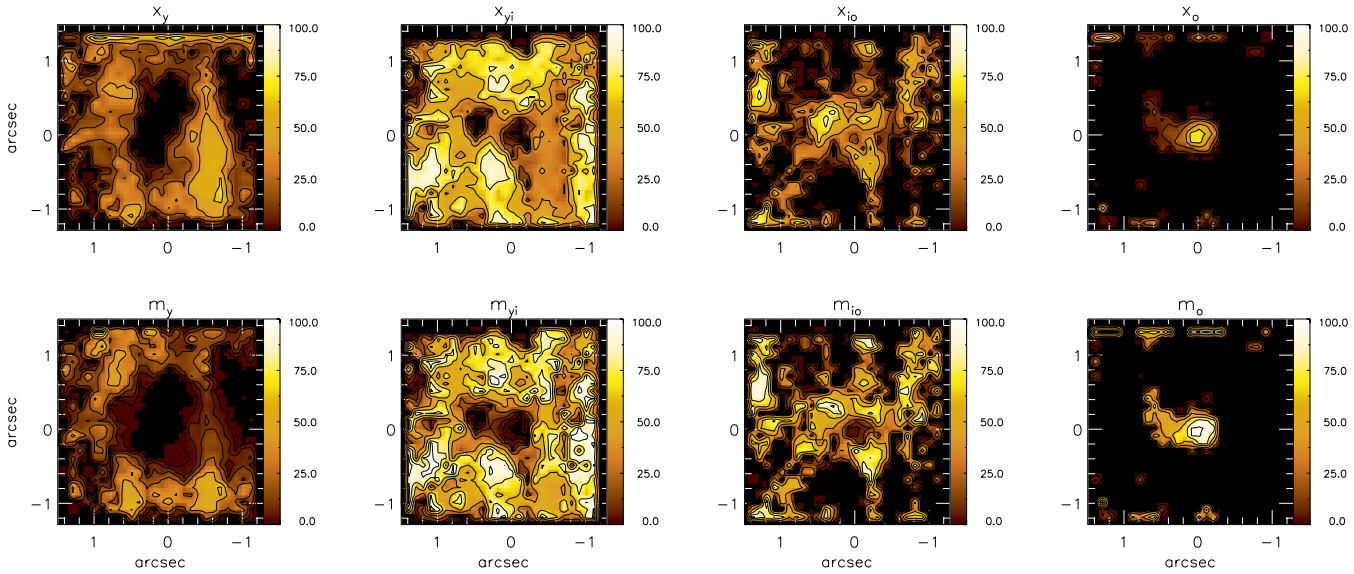

Figure 4. Spatial distributions of the per cent contribution of each SPC to the flux at $\lambda = 2.12$ μm (x_j) and to the mass (m_j), where j represents the age of the SPC: young (y: ≤ 100 Myr), young intermediate (yi: 0.3–0.7 Gyr), intermediate old (io: 1–2 Gyr) and old (o: 5–13 Gyr).

of the older ages is enhanced, particularly within 0.4 arcsec from the nucleus.

Besides the SPC distributions, STARLIGHT outputs the average reddening of the SPs (see Fig. 7 shown later). The highest values of $E(B-V) = 0.7$ [we used $A_V = 3.1E(B-V)$] are reached at the nucleus up to within ∼0.2 arcsec from it.

The goodness of the fit is measured in STARLIGHT by the per cent mean deviation: $adev = |O_\lambda - M_\lambda|/O_\lambda$, where O_λ is the observed spectrum and M_λ is the fitted model (Cid Fernandes et al. 2004, 2005b). The *adev* map for Mrk 1157 is shown later in Fig. 7 and presents values $adev \lesssim 5$ per cent at most locations, indicating that the model reproduces very well the observed underlying spectra.

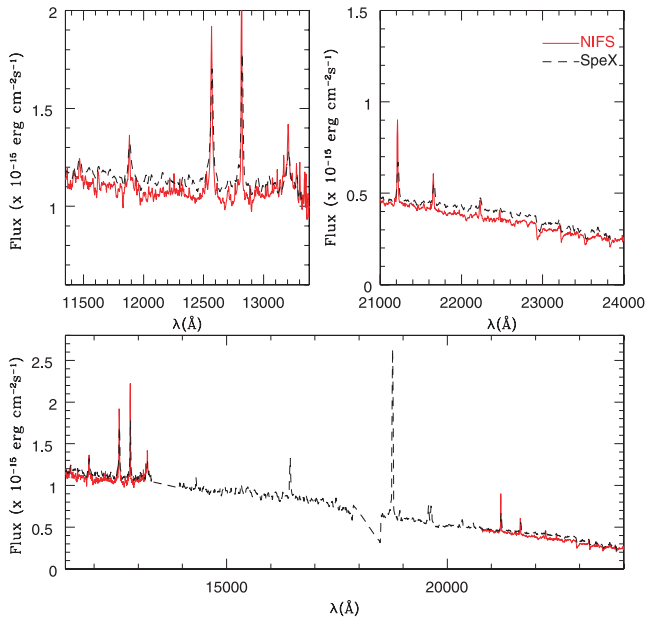

Figure 5. Comparison of the overall shape of our NIFS spectra with the SpeX cross-dispersed spectrum of Riffel, Rodríguez-Ardila & Pastoriza (2006).

We point out that, in order to have a robust result on SP fitting with STARLIGHT, it is important to have a reliable flux calibration (see the STARLIGHT manual). In other words, the fit depends on the overall shape of the observed spectrum from the J to the K band, and our NIFS observations miss the H band. In order to verify the reliability of our flux calibration, we have extracted a spectrum from our data cubes matching the aperture and position angle of our SpeX cross-dispersed spectrum (Riffel et al. 2006). Note that the SpeX data were taken in the cross-dispersed mode and thus are free from seeing and aperture effects (see Riffel et al. 2006, for details). The comparison between both spectra is shown in Fig. 5. It is clear that our NIFS spectra have a reliable flux calibration. In fact, the difference between the NIFS and SpeX spectra is lower than 3 per cent in the J band. In addition, we have performed a simulation varying the flux of the J band by 20 per cent (from 90 up to 110 per cent), and the difference from the population vector components is, in mean, $\lesssim$5 per cent, indicating that our results are robust.

5 DISCUSSION

In general, our results are similar to those obtained in the 2D mapping of the SP of Mrk 1066 (Riffel et al. 2010) as well as for previous NIR studies using single-aperture nuclear spectra (Riffel et al. 2009d). By mapping the SP in 2D, we can analyse the spatial variations of the SPCs in the inner few hundred parsecs of the galaxy. Further, the significance of these variations is enhanced by the comparison with the σ_* map presented in Fig. 6. This map was obtained by fitting the K-band CO absorption band heads with the penalized Pixel Fitting method of Cappellari & Emsellem (2004) using as stellar template spectra those of the Gemini library of late-spectral-type stars observed with the NIFS IFU (Winge et al. 2009). More details on the stellar kinematics of the central region of Mrk 1157 can be found in Riffel & Storchi-Bergmann (in preparation). The σ_* map shows a partial ring of low-σ_* values (≈50–60 km s^{-1}) surrounding the nucleus at ≈0.8 arcsec (230 pc) from it, immersed in higher σ_* values of the bulge stars (≈100 km s^{-1}).

Such rings are commonly observed in the central region of active galaxies and are due to kinematically colder regions with

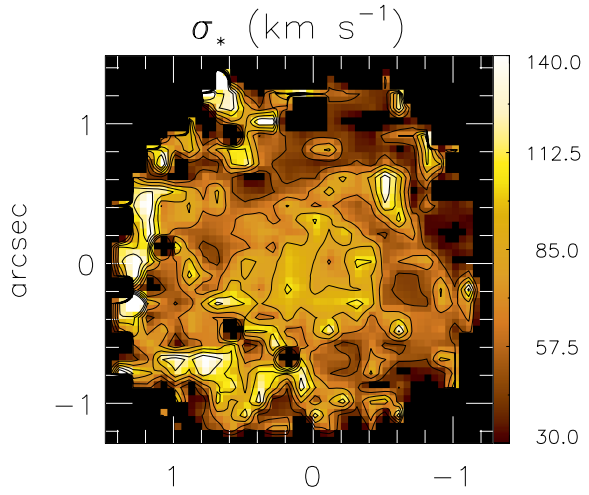

Figure 6. Stellar velocity dispersion map from Riffel & Storchi-Bergmann (in preparation).

younger stars than the underlying bulge (Barbosa et al. 2006; Deo, Crenshaw & Kraemer 2006; Simões Lopes et al. 2007; Riffel et al. 2008a, 2009a). The comparison between Mrk 1157 SP synthesis maps (light- and mass-weighted) and the σ_* map shows that the low-σ_* ring is spatially correlated with the young-intermediate-age SPC, while the highest σ_* rings are associated with the old component. Interestingly, very similar results were found by Riffel et al. (2010) for Mrk 1066. Thus, the results found for Mrk 1157 and Mrk 1066 support the use of low stellar velocity dispersion as a tracer of young-intermediate-age stars in the galaxy centre, thus confirming the interpretation of the above studies.

The most compressed form to represent the SPC mixture of a galaxy is by its mean stellar age, which was defined by Cid Fernandes et al. (2005b) in two ways: the first is weighted by the light fraction,

$$\langle \log t_\star \rangle_{\rm L} = \sum_{j=1}^{N_\star} x_j \log t_j, \quad (5)$$

and the second weighted by the stellar mass fraction,

$$\langle \log t_\star \rangle_{\rm M} = \sum_{j=1}^{N_\star} m_j \log t_j. \quad (6)$$

Being both definitions limited by the age range used in our base, the former is more representative of the younger ages, while the latter is enhanced by the old SPC (Riffel et al. 2009d). In order to compare our results with those derived using integrated spectra, we have calculated the mean ages for the central region of Mrk 1157. These mean ages in light and mass fractions are $\langle \log t_\star \rangle_{\rm L} = 8.48$ $\langle \log t_\star \rangle_{\rm M} = 8.65$, respectively. Note that these values were obtained taking the mean value over all the spectra in the map (e.g. summing $\langle \log t_\star \rangle_{\rm L}$ values over the map and dividing the result by the number of spectra in the map).

Besides our study of Mrk 1066 (Riffel et al. 2010), to date, the only previous 2D SP studies of active galaxies in the NIR are those from the group of R. I. Davies. Davies et al. (2007) investigated the circumnuclear star formation in nine Seyfert galaxies using the NIR adaptive optics integral field spectrograph SINFONI at the Very Large Telescope. Based on measurements of the Brγ emission-line equivalent width, supernova rate and mass-to-light ratio, these authors found circumnuclear discs of typical diameters of tens of pc with a 'characteristic' age in the range 10–300 Myr. Such a 'characteristic' age can be associated with our mean age (∼300 Myr); thus, our result for Mrk 1157 is in good agreement with those found by Davies et al. (2007) for their sample (which does not include Mrk 1157). Nevertheless, as pointed out by Riffel et al. (2010), the methodology adopted here allowed us not only to obtain a 'characteristic' age, but also to map the spatial distribution of the SPCs of different ages in the central region of a Seyfert galaxy, on the basis of NIR integral-field spectroscopy. Moreover, our results are in reasonable agreement with those of Riffel et al. (2009d) where the authors use integrated long-slit spectroscopy (considering the different apertures).

In further support to the results of the synthesis, we found that the average reddening map derived for the SP (Fig. 7) is in close agreement with the one derived for the narrow-line region using emission-line ratios (Riffel & Storchi-Bergmann, in preparation), presenting a similar structure and a very similar average value to that found by Riffel et al. (2009d, $E(B-V) \approx 0.63$) for the SP, using NIR-integrated spectra.

6 CONCLUSIONS

As part of an ongoing project aimed at mapping the age distribution of the NIR SP in the inner few hundred parsecs of Seyfert galaxies, we present the spectral synthesis for the nuclear region of the Seyfert 2 galaxy Mrk 1157 (NGC 591) within the inner ∼400 pc at a spatial resolution of ≈35 pc. We have used a cleaning method which allowed us to remove the noise effects and redundant data from the 1D extractions, thus allowing a more accurate analysis of the SPCs. Using the noise-free cube, we have mapped the

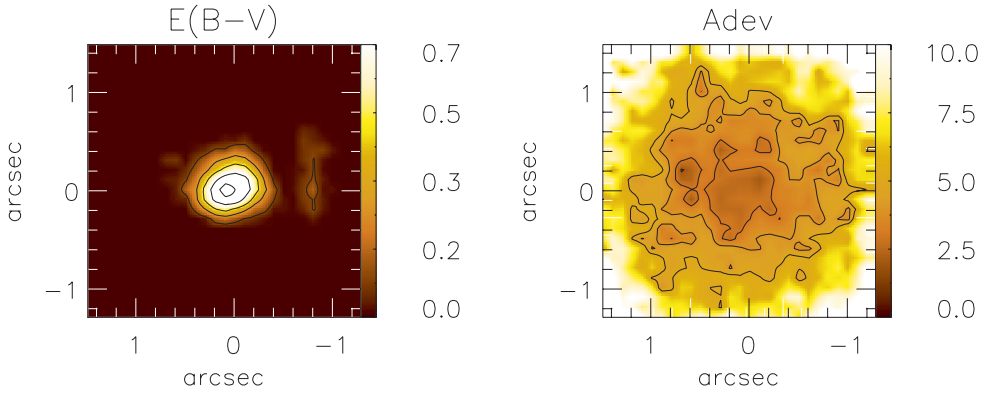

Figure 7. Reddening map and *adev* map (per cent mean deviation from the spectral fit).

distribution of SPCs of different ages, and of their average reddening. The main conclusions of this work are as follows:

(i) The cleaning technique presented here has allowed us to perform the spectral synthesis in noisy spectra (e.g. borders of the data cube) in a more accurate way.

(ii) The age of the dominant SP presents spatial variations: the flux and mass contributions within the inner ≈160 pc are dominated by old stars ($t \geq 5$ Gyr), while intermediate-age stars ($0.3 \leq t \leq 0.7$ Gyr) dominate in the circumnuclear region between 170 and 350 pc.

(iii) As for Mrk 1066 (Riffel et al. 2010), we found that there is a spatial correlation between the distribution of the intermediate-age component and low stellar velocity dispersion values, which delineates a partial ring around the nucleus of Mrk 1157. Similar structures have been found around other active nuclei, and our results for Mrk 1157 (and Mrk 1066) reveal that these nuclear rings are formed by intermediate-age stars.

(iv) No signatures of non-thermal and hot dust components are found in the central region of Mrk 1157.

ACKNOWLEDGMENTS

We thank an anonymous referee for helpful suggestions. The STARLIGHT project is supported by the Brazilian agencies CNPq, CAPES and FAPESP, and by the France-Brazil CAPES/Cofecub program. This work is based on observations obtained at the Gemini Observatory, which is operated by the Association of Universities for Research in Astronomy, Inc., under a cooperative agreement with the NSF on behalf of the Gemini partnership: the National Science Foundation (United States), the Science and Technology Facilities Council (United Kingdom), the National Research Council (Canada), CONICYT (Chile), the Australian Research Council (Australia), Ministério da Ciência e Tecnologia (Brazil) and southeastCYT (Argentina). This research has made use of the NED which is operated by the Jet Propulsion Laboratory, California Institute of Technology, under contract with the National Aeronautics and Space Administration. This work has been partially supported by the Brazilian institution CNPq.

REFERENCES

Asari N. V., Cid Fernandes R., Stasińska G., Torres-Papaqui J. P., Mateus A., Sodré L., Schoenell W., Gomes J. M., 2007, MNRAS, 381, 263
Barbosa F. K. B., Storchi-Bergmann T., Cid Fernandes R., Winge C., Schmitt H., 2006, MNRAS, 371, 170.
Bruzual G., Charlot S., 2003, MNRAS, 344, 1000
Cappellari M., Emsellem E., 2004, PASP, 116, 138
Cardelli J. A., Clayton G. C., Mathis J. S., 1989, ApJ, 345, 245
Cid Fernandes R., Gu Q., Melnick J., Terlevich E., Terlevich R., Kunth D., Rodrigues Lacerda R., Joguet B., 2004, MNRAS, 355, 273
Cid Fernandes R., Mateus A., Sodré, Laerte, Stasińska G., Gomes J. M., 2005a, MNRAS, 358, 363.
Cid Fernandes R., González Delgado R. M., Storchi-Bergmann T., Martins L. P., Schmitt H., 2005b, MNRAS, 356, 270
Cid Fernandes R. et al., 2009, Rev. Mex. Astron. Astrofis. Conf. Ser., 35, 127
Davies R. I. et al., 2006, ApJ, 646, 754
Davies R. I., Sánchez F. M., Genzel R., Tacconi L. J., Hicks E. K. S., Friedrich S., Sternberg A., 2007, ApJ, 671, 1388
Deo R. P., Crenshaw D. M., Kraemer S. B., 2006, AJ, 132, 321
Dors O. L., Jr, Storchi-Bergmann T., Riffel R. A., Schimdt A. A., 2008, A&A, 482, 59
González Delgado R. M., Heckman T., Leitherer C., 2001, ApJ, 546, 845
Heckman T. M., 2004, in Ho L., ed., Co-evolution of Black Holes and Galaxies. Cambridge Univ. Press, Cambridge, p. 358
Heckman T. M., González Delgado R. M., Leitherer C., Meurer G. R., Krolik J., Wilson A. S., Koratkar A., Kinney A., 1997, ApJ, 482, 114
McGregor P. J. et al., 2003, in Iye M., Moorwood A. F. M., eds, SPIE Proc. Vol. 4841, Instrument Design and Performance for Optical/Infrared Ground-based Telescopes. SPIE, Bellingham, p. 1581
Malkan M. A., Gorjian V., Tam R., 1998, ApJS, 117, 25
Mallat S., 1999, A Wavelet Tour of Signal Processing, 2nd edn. Academic Press, New York
Maraston C., 2005, MNRAS, 362, 799
Martins L., Riffel R., Rodríguez-Ardila A., Gruenwald R., de Souza R., 2010, MNRAS, 406, 2185
Mateus A., Sodré L., Cid Fernandes R., Stasińska G., Schoenell W., Gomes J. M., 2006, MNRAS, 370, 721
Norman C., Scoville N., 1988, ApJ, 332, 124
Riffel R. A., Storchi-Bergmann T., 2011, MNRAS, 411, 469
Riffel R., Rodríguez-Ardila A., Pastoriza M. G., 2006, A&A, 457, 61
Riffel R., Pastoriza M. G., Rodríguez-Ardila A., Maraston C., 2007, ApJ, 659, 103
Riffel R. A., Storchi-Bergmann T., Winge C., McGregor P. J., Beck T., Schmitt H., 2008a, MNRAS, 385, 1129
Riffel R., Pastoriza M. G., Rodríguez-Ardila A., Maraston C., 2008b, MNRAS, 388, 803
Riffel R. A., Storchi-Bergmann T., Dors O. L., Winge C., 2009a, MNRAS, 393, 783
Riffel R. A., Storchi-Bergmann T., McGregor P. J., 2009b, ApJ, 698, 1767
Riffel R. A., Storchi-Bergmann T., Dors O. L., Winge C., 2009c, MNRAS, 393, 783
Riffel R., Pastoriza M. G., Rodríguez-Ardila A., Bonatto C., 2009d, MNRAS, 400, 273
Riffel R. A., Storchi-Bergmann T., Riffel R., Pastoriza M. G., 2010, ApJ, 713, 469
Riffel R., Bonatto C., Cid Fernandes R., Pastoriza M. G., Balbinot E., 2011, MNRAS, 411, 1897
Rodríguez-Ardila A., Riffel R., Pastoriza M. G., 2005, MNRAS, 364, 1041
Rodríguez-Ardila A., Prieto M. A., Viegas S., Gruenwald R., 2006, ApJ, 653, 1098
Simões Lopes R. D., Storchi-Bergmann T., de Fátima Saraiva M., Martini P., 2007, ApJ, 655, 718
Starck, J. L., Murtagh, F., 2006, Astronomical Image and Data Analysis, 2nd edn. Springer-Verlag, Berlin
Steiner J. E., Menezes R. B., Ricci T. V., Oliveira A. S., 2009, MNRAS, 395, 64
Storchi-Bergmann T., Raimann D., Bica E. L. D., Fraquelli H. A., 2000, ApJ, 544, 747
Storchi-Bergmann T., González Delgado R., Schmitt H., Cid Fernandes R., Heckman T., 2001, ApJ, 559, 147
Storchi-Bergmann T., McGregor P., Riffel R. A., Simões Lopes R., Beck T., Dopita M., 2009, MNRAS, 394, 1148
Terlevich E., Diaz A. I., Terlevich R., 1990, MNRAS, 242, 271
Winge C., Riffel R. A., Storchi-Bergmann T., 2009, ApJS, 185, 186

This paper has been typeset from a TEX/LATEX file prepared by the author.